ADIABATIC RELAXATION OF CONVECTIVE-DIFFUSIVE GAS TRANSPORT IN A POROUS FUEL CELL ELECTRODE*

KEITH PROMISLOW† AND JOHN M. STOCKIE‡

Abstract. The gas diffusion layer in the electrode of a proton exchange membrane fuel cell is a highly porous material which acts to distribute reactant gases uniformly to the active catalyst sites. We develop a mathematical model for flow of a multicomponent mixture of ideal gases in a highly porous electrode. The model is comprised of a porous medium equation for the evolution of the gas mixture and a singularly perturbed convection–diffusion equation for the interspecies mass transfer within the mixture. The equations are coupled through nonlinear boundary conditions which describe consumption of reactants and generation of end products at the catalyst layer. Through a two time-scale analysis, we derive a single reduced equation which captures the slow, diffusively-driven, adiabatic relaxation to the steady state at each electrode. The asymptotic results are compared with one- and two-dimensional computations of the full system.

Key words. multicomponent gas, convection-diffusion, porous medium, multi-scale analysis, singular perturbation, fuel cell electrode.

AMS subject classifications. 35B40, 35K55, 76R99, 76S05

1. Introduction.

In many industrial and biological applications, transport of reactant gases takes place across a thin layer of porous material. Here we consider the electrodes of a proton exchange membrane (or PEM) fuel cell, in which reactant gases are distributed to catalyst sites through a sheet of carbon fiber paper known as the *gas diffusion layer* or GDL. The consumption of reactant gases (H_2 and O_2) and generation of end products (H_2O) create gradients in component concentration across the thickness of the paper. The resulting component diffusion engenders a convective Darcy's law flow inside the porous layer, which interacts with the diffusive motion. The convective time scales are much faster than diffusive ones in the full nonlinear problem, and diffusion represents a singular perturbation to convection. Indeed our model is distinguished from similar multicomponent problems in groundwater transport by this scaling, arising from the thinness of the domain and the high porosity of the GDL. We capture the competition between convective and diffusive effects, demonstrating that the slow transients related to the relaxation of these nonlinear equations are accurately described by a single diffusion equation with a non-local convective term.

The cathode and the anode sides of a PEM fuel cell are characterized by distinct scalings, each possessing a nonlinearly stable, steady state solution. We derive asymptotic expressions for the impact of convection on the net reactant delivered across the gas diffusion layer, and provide a detailed description of the relaxation onto the steady states. On the fast time scale a convective transient governs the concentration gradient of the overall gas mixture. On the slow, diffusive time scale the convective flow relaxes adiabatically to its diffusively-driven steady state. In the anode scaling, the adiabatic equations governing the reactant concentrations are diffusively dominated,

*This work was funded by a grant from Ballard Power Systems through the MITACS National Centre of Excellence.

†Department of Mathematics and Statistics, Simon Fraser University, Burnaby, British Columbia, Canada, V5A 1S6 (kpromisl@sfu.ca).

†Department of Mathematics and Statistics, University of New Brunswick, Fredericton, New Brunswick, Canada, E3B 5A3 (stockie@math.unb.ca).

To appear in *SIAM J. Appl. Math.*

while in the cathode scaling a nonlinear, nonlocal convection term appears at leading order.

Our analysis should be of particular interest to fuel cell researchers, affording a substantial simplification of a complex, nonlinear process. Most efforts at modeling and simulating fuel cells in the literature to date have focused on the entire fuel cell, including charge, heat and mass transport. Despite the complexity of these coupled models, extensive one- and two-dimensional numerical simulations yield concentration profiles that vary linearly through the thickness of both the GDL and PEM [4, 9, 19, 26]. The reduced adiabatic model developed herein captures precisely this effect (refer to Eqs. (4.21) and (4.40)). Moreover, by deriving equations that govern the adiabatic relaxation onto the steady states, we can distinguish the significant dynamics of the system, including intermediate transients, while eliminating the stiffness which may plague numerical simulations of the fuel cell system.

Our modeling approach focuses solely on the GDL, decoupling each electrode from the rest of the fuel cell. This permits classification of different operational regimes inside the GDL based on the boundary conditions and parameters which mimic the remainder of the fuel cell. Indeed, previous modeling efforts have focused on the proton exchange membrane, despite experimental studies which strongly link fuel cell performance to geometry and material composition of the porous gas diffusion layer [2, 6].

In the next section, we discuss the physical assumptions in our GDL model and derive equations of mass transport. One of the key aspects in the model is the parameters which appear in the boundary conditions; these describe the operating conditions within the fuel cell. Section 3 presents the derivation and scaling of the equations and boundary conditions. The different scalings associated with the anode and cathode operation are of primary importance in the non-dimensionalization procedure. The analysis of a one-dimensional version of the GDL model is presented in Section 4, including derivation of the adiabatic equation and analysis of the nature of the convergence of the full system to steady state. The analytical results are verified by numerical experiments in Section 5 and conclusions are drawn regarding the applicability of the model to two-dimensional geometries that arise in fuel cells.

2. Model Derivation.

2.1. Fuel Cell Overview. A cross-section of a PEM fuel cell, depicting the major components, is shown in Fig. 2.1. The membrane–electrode assembly, or MEA, is sandwiched between two graphite plates (shaded in the diagram at left) into which are etched flow channels for oxygen gas at the cathode (top) and hydrogen at the anode (bottom). Inside the channels, a pressure gradient initiates the flow of gases, while consumption of reactants and generation of end products lead to variations in component concentrations. We introduce a coordinate system in which x denotes distance along the lateral direction in the MEA, y is measured along the height of a channel and through the thickness of the MEA, and z denotes distance along the length of a flow channel.

In the middle of the cell is a *proton exchange membrane* or PEM, composed of a polymer material, which is permeable to small, positively-charged ions. On each side of the PEM is attached a layer of carbon fiber paper, called a *gas diffusion layer* or GDL. The boundary between the PEM and GDL is loaded with a platinum catalyst that facilitates the reactions. The electric current in a fuel cell is derived from the two reactions listed at the right of Fig. 2.1. Hydrogen ions generated at the anode

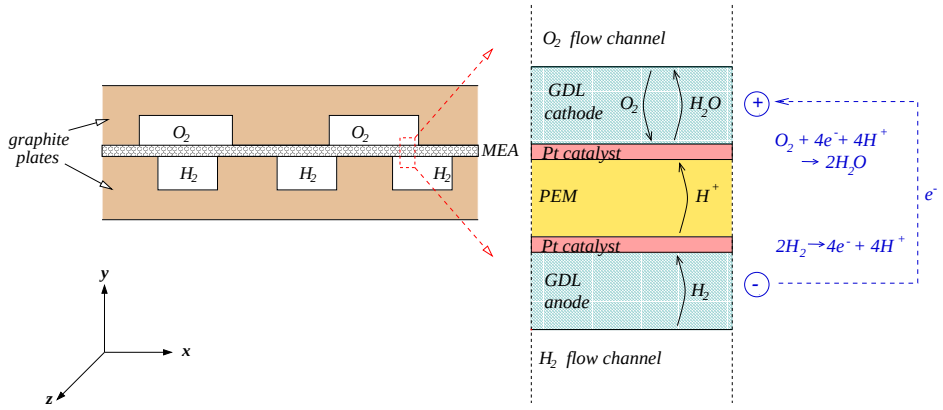

FIG. 2.1. *A proton exchange membrane fuel cell and its component parts. On the left is a cross-sectional view of the cell, showing the MEA sandwiched between the oxygen and hydrogen flow channels. The in-channel gas flow is directed normal to the page. On the right is an expanded view of the MEA. The reaction occurring at each electrode is listed on the far right, along with the flow of electrons generated when the anode and cathode are linked in an external circuit.*

catalyst layer migrate across the PEM, where they react with oxygen gas at the upper catalyst layer to produce water vapor.

2.2. Geometry and Assumptions. We focus our attention on the GDL for which we consider a two-dimensional cross-section, labeled Ω in Fig. 2.2. The lower

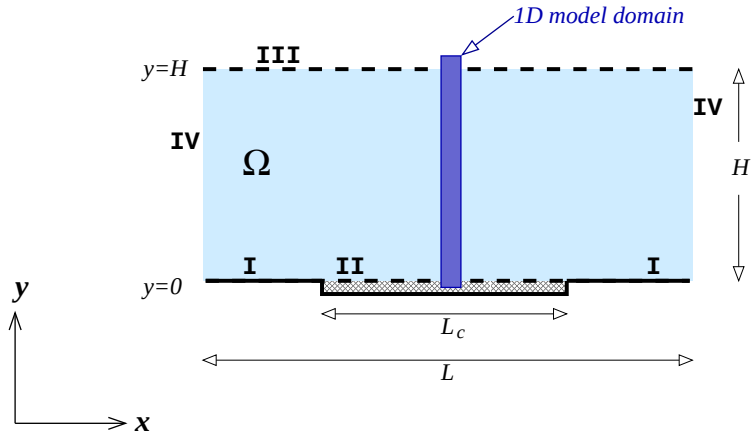

FIG. 2.2. *Dimensions of the model domain Ω: length (L), GDL thickness (H), and channel width (L_c). The boundary components are identified with Roman numerals* I–IV.

boundary of Ω, at $y = 0$, represents the interface between the GDL and either the graphite plate or an open, gas-filled, flow channel. The upper boundary, at $y = H$, corresponds to the catalyst layer separating the GDL and the PEM. The transport of ions and water within the MEA as well as the convective flow within the gas channels will not be modeled here. The coupling of the GDL to the rest of the fuel cell, including such effects as variation in reactant concentration along the length of the flow channel, nonuniformity of component concentrations in the channel, boundary layers at the porous GDL–channel interface, and dissociation rates at the catalyst

layer will be accounted for through the boundary conditions.

The channel gases are comprised of many species; indeed the O_2 flow is typically ambient air with significant amounts of nitrogen and water vapor. Proper modeling of diffusive effects requires the Maxwell–Stefan equations [12], however we substantially reduce the technical complexity of our analysis by employing Fick's model of diffusion. This approximation introduces only small quantitative differences as indicated by our preliminary calculations. We gather below the principle assumptions and simplifications we make in our model:

- Our model is isothermal and does not include transport of charge and heat. While these effects are important to overall fuel cell operations (and particularly water management), they do not have a leading order effect on the convective-diffusive transport of reactants.
- We assume all water vapor remains in the gas phase.
- All non-reacting gas species (*e.g.*, N_2 on the cathode side) have constant mole fractions.
- The inlet-to-outlet pressure drop in the channel may engender a small z–component in the GDL flow velocity which we assume to be uniform. Our focus is on the x– and y–components of the flux.
- All reactants are immediately consumed upon reaching the PEM, so that the limiting factor is mass transport in the GDL.
- External body forces such as gravity can be neglected.

2.3. Governing Equations. Models for convective–diffusive gas transport in porous media have been developed for applications arising in a wide range of fields including electrochemistry [13], flow in insulating materials [25], and groundwater transport [1], to name a few. The standard approach is to couple a mass transport equation for the mixture (typically Darcy's Law or some appropriate modification thereof) with an equation governing inter-component diffusion within the mixture. Diffusive transport is frequently modeled using Fick's Law, which is the approach taken here. However, Fick's Law is strictly valid only for binary mixtures, and for some mixtures of three or more components, the Maxwell–Stefan equations are required to obtain physically reproducible results [12].

Similar models have appeared in the fuel cell context, in which equations describing multicomponent gas flow in the GDL are coupled with equations for heat and charge transport occurring in the other fuel cell components. With the important exception of the boundary conditions, the GDL model we develop below is similar to that in [9] or [26].

We present the governing equations for the gas mixture, described by the concentrations C_1, C_2, and C_3. We denote by C_1 the concentration of reactant gas, which is H_2 on the anode side and O_2 at the cathode. At both anode and cathode, C_2 refers to water vapor concentration, while C_3 denotes any non-reacting gases, principally N_2 on the cathode side and CO_2 on the anode side. We assume that the non-reacting gas concentration C_3 is a fixed proportion, $(1 - \gamma_r)$, of the total gas concentration, $C = C_1 + C_2 + C_3$. This assumption is supported by multi-component numerical simulations which show a variation in the mole fraction C_3/C of about 2% at steady state, compared to 20% variation for C_1/C and C_2/C. Thus we may write

$$C_1 + C_2 = \gamma_r C, \tag{2.1}$$

where the constant γ_r is determined by concentration values inside the channel. In what follows, (2.1) will be used to eliminate the variable C_2 in favor of the total

mixture concentration C.

The conservation of mass for the gas mixture takes the form

$$\frac{\partial C}{\partial t} + \nabla \cdot (C\boldsymbol{U}) = 0, \tag{2.2}$$

where $\boldsymbol{U}$ is the molar-averaged mixture velocity. The transport of individual reactants is significantly affected by inter-component diffusion. The conservation law for the reactant concentration takes the form

$$\frac{\partial C_1}{\partial t} + \nabla \cdot \underbrace{(C_1\boldsymbol{U} + \boldsymbol{J}_1)}_{\boldsymbol{N}_1} = 0, \tag{2.3}$$

where $\boldsymbol{J}_1$ is the diffusive flux (measured relative to the molar-averaged velocity) and $\boldsymbol{N}_1$ is the total (convective plus diffusive) flux of the first component.

The diffusive flux is given by Fick's law, which states that the flux of one component relative to the molar averaged velocity is proportional to the gradient in mole fractions via

$$\boldsymbol{J}_1 = -CD\nabla\left(\frac{C_1}{C}\right), \tag{2.4}$$

where D is the diffusivity. There are several other equivalent forms of Fick's Law, which vary depending on the averaging procedure used to obtain a mixture velocity [5, 22]. The form of Eq. (2.4) is tied to our choice of a molar-averaged velocity, which is consistent with the treatment of flow of gases in porous media by others in the engineering literature [7, 20]. Darcy's Law gives the mixture velocity in terms of the pressure P as

$$\boldsymbol{U} = -\frac{K}{\varepsilon_p \mu}\nabla P, \tag{2.5}$$

where μ is the viscosity of the mixture, and the GDL material is characterized by the parameters K (permeability) and ε_p (porosity). The coefficients K and D are actually tensor quantities because the fibrous GDL material is anisotropic; however, we will assume for the sake of simplicity that the GDL is isotropic, taking K and D as scalars. The validity of Darcy's law is subject to the assumptions that boundary effects are negligible, and that the gas velocity is small enough that inertial terms can be neglected [17]. The latter is clearly satisfied in the GDL since the pore Reynolds number is small (*i.e.*, $Re_p = \rho U\sqrt{K}/\mu \ll 1$), and the boundary layer between channel and GDL has a thickness on the order of one pore width [9].

The final relation needed to close the system is a constitutive equation for the gas mixture. Assuming the gas to be ideal and adiabatic, the pressure depends linearly on the concentration,

$$P = C\mathcal{R}\mathcal{T}, \tag{2.6}$$

where $\mathcal{R}$ is the universal gas constant and $\mathcal{T}$ is the temperature. While there are significant temperature variations within a fuel cell, we will take the system to be isothermal, an assumption that is commonly made in other fuel cell models ([26] and [4], for example).

Eqs. (2.2)–(2.6) together form a coupled system of nonlinear PDEs for the concentrations C and C_1. This is most easily seen by substituting expressions (2.4)–(2.6) into the conservation Eqs. (2.2) and (2.3) to obtain

$$\frac{\partial C}{\partial t} - \nabla \cdot [\Gamma\, C \nabla C] = 0, \tag{2.7a}$$

$$\frac{\partial C_1}{\partial t} - \nabla \cdot \left[\Gamma\, C_1 \nabla C + DC \nabla \left(\frac{C_1}{C}\right)\right] = 0, \tag{2.7b}$$

where $\Gamma \doteq \dfrac{K\mathcal{R}\mathcal{T}}{\varepsilon_p \mu}$ is a constant. The relative importance of convection and diffusion, determined by the parameters Γ and D, is critical in determining the behavior of solutions. We will discuss this issue and the importance of an appropriate rescaling of the equations in Section 3.

2.4. Boundary Conditions. The boundary consists of four distinct components, labeled I–IV in Fig. 2.2. We derive the boundary conditions on each of the four sections as follows:

I. The impermeable boundary at $y = 0$ between the graphite plate and the GDL where there can be no flux of reactant, either by diffusion or convection, in the direction normal to the wall. This translates into the following conditions on the y-component of the fluxes

$$J_1^y = 0 \qquad \text{and} \qquad N_1^y = 0,$$

which are equivalent to the following Neumann conditions on the concentrations

$$\frac{\partial}{\partial y}\left(\frac{C_1}{C}\right) = 0 \qquad \text{and} \qquad \frac{\partial C}{\partial y} = 0. \tag{2.8}$$

II. The permeable boundary at $y = 0$, where the mixture concentration immediately inside the GDL is taken to be identical to that in the channel:

$$C = \overline{C}, \tag{2.9a}$$

that is, we assume the pressure to be uniform throughout the depth of the channel.

We assume further that the diffusive flux of the first component across the channel/GDL interface is proportional to the difference in concentrations on either side:

$$J_1^y = r_0(\overline{C}_1 - C_1).$$

Here $\overline{C}_1$ is a depth-averaged channel concentration and r_0 can be interpreted as a *mass transfer coefficient*. Using (2.9a), this expression can be rewritten entirely in terms of the concentrations as

$$\frac{\partial}{\partial y}\left(\frac{C_1}{C}\right) = -\frac{r_0}{D\overline{C}}(\overline{C}_1 - C_1). \tag{2.9b}$$

An estimate for r_0 can be obtained from the Sherwood number, $Sh = r_0 L_d / D$, where L_d is a characteristic length that we take proportional to the channel depth. The Sherwood number is typically obtained experimentally and values are available in the literature (see [3] and the references therein).

III. The permeable boundary at $y = H$, between the catalyst and GDL, where a similar condition to (2.9b) is applied

$$J_1^y = r_{_H}\,(C_1 - 0).$$

The mass transfer coefficient $r_{_H}$ models the reactions and electrochemistry taking place in the catalyst region. It is tuned to match net flux to experimental values determined from averaged current densities. We consider the catalytic reaction to be instantaneous and irreversible, which leads to a choice of zero concentration in the catalyst layer. Using the definition of the diffusive flux, the condition above can be rewritten as

$$\frac{\partial}{\partial y}\left(\frac{C_1}{C}\right) = -\frac{r_{_H} C_1}{DC}. \tag{2.10a}$$

The second boundary condition on III arises from a *return flux* of the end product component which is proportional to that of the reactant

$$N_2^y = (\nu - 1)\, N_1^y.$$

The parameter ν is a *return coefficient* that determines the direction and magnitude of the product H_2O component flux. We assume that at steady state the majority of water vapor manufactured at the cathode catalyst layer remains on the cathode side. Since two water molecules are produced by the reaction for every O_2 molecule consumed, but only one H_2O for every H_2 molecule, we take $-1 \le \nu < 0$ at the cathode and $0 < \nu \le 1$ at the anode. Indeed, taking $\nu = -1$ at the cathode corresponds to the situation where all water produced remains at the cathode in the vapor state, while $-1 < \nu$ corresponds to either some loss of water vapor to the liquid state or transfer of water vapor to the anode. The boundary condition above may be rewritten as a Neumann condition involving the concentrations:

$$\frac{\partial C}{\partial y} = -\frac{\nu r_{_H} C_1}{\Gamma\,(\gamma_r C - \nu C_1)}. \tag{2.10b}$$

IV. The open side boundaries ($x = 0$ and $x = L$), where we assume that the solution is periodic in x.

3. Non-Dimensionalization. We now seek to identify the mechanisms that dictate the balance between convection- and diffusion-induced fluxes, and the differing time scales on which the two fluxes operate. The units and approximate magnitude of each of the parameters appearing in the problem are listed in Table 3.1. In the remainder of this paper, we use the dimensionless variables obtained by scaling C by $\overline{C}$, x and y by H, and introducing the rescaled "convective time", $\tau = (\Gamma\overline{C}/H^2)\,t$, and reactant mole fraction, $R = C_1/C$. With these definitions, we arrive at the dimensionless equations

$$C_\tau - \nabla\cdot(C\nabla C) = 0, \tag{3.1a}$$

$$CR_\tau - C\nabla C\cdot\nabla R - \delta\nabla\cdot(C\nabla R) = 0. \tag{3.1b}$$

The new parameter

$$\delta = \frac{D}{\Gamma\overline{C}} \ll 1$$

can be interpreted as the reciprocal of a Péclet number (*i.e.*, $\delta \sim Pe^{-1}$). It represents the ratio of the convective ($H^2/\Gamma\overline{C}$) and diffusive (H^2/D) time scales, and defines the slow time variable, $T = \delta\tau$, that appears in the analysis of the adiabatic equation in Section 4. We have in (3.1) a porous medium equation for the concentration and a singularly perturbed convection–diffusion equation for the reactant.

For simplicity we study a one-dimensional vertical slice, shaded in Fig. 2.2, that extends from the channel at $y = 0$ to the membrane at $y = 1$. The relevant boundary conditions are (2.9) and (2.10). Physically, we would expect that this problem is a reasonable approximation to the two-dimensional problem when the channels are very wide, so that $L_c/L \approx 1$. Introducing the dimensionless parameters $\epsilon = Hr_{_H}/D$, $\beta = Hr_{_0}/D$ and $\gamma = \overline{C}_1/\overline{C}$, the boundary conditions become

$$C(0) = 1, \qquad C_y(1) = -\epsilon\delta\frac{\nu R(1)}{\gamma_r - \nu R(1)}, \tag{3.2a}$$

$$R_y(0) = -\beta(\gamma - R(0)), \qquad R_y(1) = -\epsilon R(1). \tag{3.2b}$$

These are supplemented with initial conditions

$$C(0, y) = C_0(y), \qquad R(0, y) = R_0(y). \tag{3.2c}$$

For later reference we introduce the dimensionless net flux of reactant

$$N_1 = -CR\nabla C - \delta C\nabla R, \tag{3.3}$$

which is related to its dimensional counterpart by the expression $N_1^d = N_1 \cdot \Gamma\overline{C}^2/H$. Typical values of the parameters are listed in Table 3.1 for both physical and non-dimensional quantities. Particular attention should be paid to $r_{_0}$ and $r_{_H}$, since the

TABLE 3.1
Parameter values (in cgs units) used for the GDL model.

	Parameter	**Anode** (H_2)	**Cathode** (O_2)
Domain:	H (GDL thickness, cm)	0.05	0.05
	L (domain width, cm)	1.0	1.0
	L_c (channel width, cm)	0.5	0.5
Gas properties:	Γ (convection, $cm^5/s \cdot mol$)	3.24×10^7	1.85×10^7
	D (diffusivity, cm^2/s)	0.29	0.066
	$\overline{C}$ (concentration, mol/cm^3)	3.475×10^{-5}	3.475×10^{-5}
	$r_{_0}$ (bottom transfer rate, cm/s)	3.0	0.20
	$r_{_H}$ (top transfer rate, cm/s)	0.005	0.0625
Time scales:	$t/\tau = H^2/\Gamma\overline{C}$ (fast time, s)	2.2×10^{-6}	3.9×10^{-6}
	$t/T = H^2/D$ (slow time, s)	0.0086	0.038
Nondimensional quantities:	$\delta = D/\Gamma\overline{C}$	0.00026	0.00010
	$\epsilon = Hr_{_H}/D$	0.00086	0.047
	$\beta = Hr_{_0}/D$	0.52	0.15
	$\gamma = \overline{C}_1/\overline{C}$	0.80	0.21
	$\gamma_r = (\overline{C}_1 + \overline{C}_2)/\overline{C}$	0.90	0.31–0.41[1]
	ν (return coefficient)	0.99	−1.0

[1] The range in values for γ_r represents a variation in the water vapor mole fraction from inlet to outlet as the reactant gas is consumed on the cathode side.

difference in magnitude betwen the two mass transport coefficients lends support to the separate scalings for anode and cathode boundary conditions. The quantities $D/r_{_H}$ and $D/r_{_0}$ are length scales over which diffusion operates for a given mass transport coefficient (or a given consumption). Thus, ϵ and β are measures of the ratio of diffusive length scale to the thickness of the GDL. For the anode, we have $\delta \ll 1$ and fix ϵ as a multiple of δ via $\epsilon = \epsilon_0 \delta$, with $\epsilon_0 = \mathcal{O}(1)$; this corresponds to a consumption limited state. For the cathode on the other hand, δ and ϵ are taken to satisfy the relationship $\delta \ll \epsilon \ll 1$. To obtain explicit expressions in the expansion of the adiabatic steady state solutions, we assume that β and γ are comparable in size to ϵ, so that $\beta = \beta_0 \epsilon$ and $\gamma = \gamma_0 \epsilon$, where $\beta_0, \gamma_0 = \mathcal{O}(1)$.

4. Adiabatic Relaxation. A great deal of analytical work has appeared in the literature for the porous medium equation, which is our Eq. (3.1a) governing the mixture concentration. We refer the interested reader to the reviews of Kalashnikov [10] and Vazquez [24] which provide excellent overviews of the current status of the theory for this equation. We focus our analysis on the effect of coupling Eq. (3.1a) to (3.1b) for interspecies diffusion through the nonlinear boundary conditions. Similar systems arise in a host of related porous media problems involving gas transport [8], multiphase flows [23], and reaction and heat transfer in porous catalysts [13]. Analyses have been performed for related diffusion problems [11, 18], but the focus in these other works is on forced convection with passive diffusion. Our problem is unique in that it is convectively dominated, but the driving force arises primarily through diffusive processes.

In what follows, we provide a detailed description of the two-stage relaxation of the coupled system (4.4) which is obtained from (3.1) by neglecting a small transient term. We derive a Maximum Principle for the system and show that the total concentration C relaxes on the fast time scale to a quasi-steady state determined by boundary values. The reactant mole fraction R converges to steady state on the slow scale $T = \delta\tau$, but after a rapid initial transient both reactant and total concentration may be well described in terms of the solution of a single nonlinear, nonlocal, adiabatic equation (4.21). Indeed, we develop expansions for the steady states of the full system from an analysis of the reduced adiabatic equations.

As a notational convenience in this section, κ will denote a positive constant which depends upon the fixed parameters but not upon δ, ϵ, or the initial data, while A will denote any positive constant independent of δ and ϵ, whose value may change from line to line. We use $\|\cdot\|_p$ to denote the L^p norm, $\|\cdot\|_\infty$ the L^∞ norm, and the H^1 norm takes the form $\|\cdot\|_{H^1} = [\|\cdot\|_2^2 + \|\frac{\partial}{\partial y}(\cdot)\|_2^2]^{1/2}$.

We simplify the study of equation (3.1) and (3.2) by introducing new dependent variables which satisfy homogeneous boundary conditions, namely

$$M(\tau, y) = C(\tau, y) - (1 + \delta f(R(\tau, 1))y)\,, \tag{4.1a}$$

$$N(\tau, y) = R(\tau, y) - R_b(y), \tag{4.1b}$$

where $f(z) = -\epsilon \frac{\nu z}{\gamma_r - \nu z}$ and

$$R_b(y) = r_1 - r_2 y, \tag{4.2}$$

with $r_1 = \dfrac{\beta\gamma(1+\epsilon)}{\epsilon + \beta(1+\epsilon)}$ and $r_2 = \dfrac{\epsilon\beta\gamma}{\epsilon + \beta(1+\epsilon)}$. For notational convenience we denote $f(R(\tau, 1))$ by $f(R)$ or simply f when this presents no ambiguity. In these new variables

we have

$$M_\tau = C_\tau + \delta\, f'(R(1))\, R_\tau(1)\, y. \tag{4.3}$$

The linear term $\delta\, f'(R(1))\, R_\tau(1)\, y$ is formally $\mathcal{O}(\delta)$, and on the slow time scale it is $\mathcal{O}(\delta^2)$ and eventually decays to zero. The inclusion of this small transient term introduces significant technicalities into the analysis, without modifying the main result, namely Theorem 4.4 and Corollary 4.5 detailing the proximity of the adiabatic form (4.40) to the full solution. Moreover the numerical results (see Figure 5.4) show excellent agreement between the full system (3.1) and the adiabatic form derived from Eqs. (4.4) below. We neglect the small transient term in (4.3), and the new variables satisfy the following equations

$$M_\tau = (M_y + \delta f)^2 + (M + 1 + \delta f y) M_{yy}, \tag{4.4a}$$
$$N_\tau = (C + \delta \ln C)_y (N_y - r_2) + \delta N_{yy}, \tag{4.4b}$$

with the boundary conditions

$$M(0) = 0, \qquad M_y(1) = 0, \tag{4.5a}$$
$$N_y(0) = \beta N(0), \qquad N_y(1) = -\epsilon N(1). \tag{4.5b}$$

In the statement and proof of the Maximum Principle, it is convenient to introduce the quantity $f_\infty \equiv \max\left\{\epsilon, \epsilon \left|\frac{\nu\gamma_1}{\gamma_r - \nu\gamma_1}\right|\right\}$ where $\gamma_1 > 0$ is defined in the lemma below.

LEMMA 4.1 (Maximum and Minimum Principle). *Let α and γ_1 be given which satisfy $1 > \alpha > 0$ and $\gamma_r > \gamma_1 > \gamma$. Then for any initial data $C_0, R_0 \in H^1$ satisfying $C_0(y) \geq \alpha + 2\delta f_\infty$ and $\gamma_1 \geq R_0(y) > 0$, the corresponding solutions C and R of (3.1) and (3.2) satisfy*

$$C(\tau, y) \geq \alpha > 0, \qquad \gamma_1 \geq R(\tau, y) \geq 0 \qquad \text{for all } y \in (0,1) \text{ and } \tau \geq 0. \tag{4.6}$$

Proof. Suppose M attains its minimum value at some smooth curve of interior points $y = \widehat{y}(\tau)$. Then $\frac{d}{d\tau} M(\tau, \widehat{y}(\tau)) = M_\tau + M_y \frac{d}{d\tau}\widehat{y} = M_\tau$, but

$$M_\tau = (M_y + \delta f)^2 + M_{yy}(M + 1 + \delta f \widehat{y}) \geq M_{yy} C.$$

It follows that any interior minimum of M is non-decreasing so long as $C > 0$. The minimum of M cannot be achieved at $y = 0$ since $M(0) = 0$ while from the boundary condition $M_y(1) = 0$, the point $y = 1$ can be a minimum of M only if $M_{yy}(1) \geq 0$, which implies $M_\tau(1) = M_{yy}(1) C(1)$. We conclude that so long as $C > 0$, the minimum value of M is non-decreasing. Rewriting (3.1b) as

$$R_\tau = (C + \delta \ln C)_y\, R_y + \delta R_{yy},$$

we find that at any interior extremal point of R we have $R_y = 0$ and $R_\tau = \delta R_{yy}$; hence, interior minima of R are non-decreasing and interior maxima are non-increasing. An examination of the boundary conditions shows R can have a local maximum at $y = 0$ only if $R(0) \leq \gamma$ and a local minimum only if $R(0) \geq \gamma$. So long as $R(1) > 0$ the point $y = 1$ can only be a local minimum; however $R(\tau, 1)$ may decrease with increasing τ, but only to the value $R(1) = 0$. Indeed if R achieves a minimum value of 0 at $y = 1$ then the boundary conditions imply $R_y(1) = 0$ and hence $R_\tau(1) = \delta R_{yy}(1) \geq 0$. Thus

we have shown that the range of R is a subset of the interval $[0,\gamma_1]$. This implies $|f(R)| \le f_\infty$. Moreover $M(\tau,y)$ is bounded from below by

$$\min_{y\in[0,1]} M(0,y) = \min_{y\in[0,1]} (C_0(y) - (1+\delta f y)) \ge \alpha - 1 + \delta f_\infty,$$

which from (4.1a) yields $C(\tau,y) \ge M(\tau,y) + (1-\delta f_\infty) \ge \alpha > 0$, for all $\tau \ge 0$. ∎

4.1. Relaxation of the Total Concentration. The slow time evolution of the total concentration C is controlled by its boundary data through the term $f(R)$.

PROPOSITION 4.2. *Let $\alpha > 0$ be as given by Lemma 4.1. There exist η_0 and δ_0 positive, such that for all initial data C_0 satisfying $\|C_{0y}\|_2 \le \eta_0$ and all $0 < \delta < \delta_0$, the solution C given by (4.1) through (4.4) satisfies*

$$\|C(\tau) - (1+\delta f(R) y)\|_{H^1} \le A\left(e^{-\kappa\tau} + \delta^2\epsilon^2\right), \qquad \text{for all } \tau \ge 0, \tag{4.7}$$

and for some κ and A both positive. Moreover, the estimate (4.7) holds in the L^2 norm for any $C_0 \in H^1$.

Proof. Multiply equation (4.4a) by M, integrate over $(0,1)$, integrate by parts and use the boundary conditions (4.5); there follows the equality

$$\frac{1}{2}\frac{d}{d\tau}\|M\|_2^2 = -\int_0^1 \left(M_y^2(1+M+\delta f y) - \delta^2 f^2 M\right)\, dy + \frac{1}{2}\delta f M^2(1). \tag{4.8}$$

From Lemma 4.1 we have $C = M + 1 + \delta f y \ge \alpha > 0$, while $|\int_0^1 M\, dy| \le \|M\|_2$; and from the L^∞ embedding $\|M\|_\infty \le \sqrt{2}\,\|M\|_2^{1/2}\,\|M_y\|_2^{1/2}$ we have $|M(1)|^2 \le 2\|M\|_2\,\|M_y\|_2$. Applying Hölder's inequality and these bounds to (4.8) yields the inequality

$$\frac{1}{2}\frac{d}{d\tau}\|M\|_2^2 \le -\alpha\|M_y\|_2^2 + \delta^2 f^2\|M\|_2 + \delta|f|\cdot\|M\|_2\,\|M_y\|_2. \tag{4.9}$$

Young's inequality applied to the last term gives the estimate

$$\frac{1}{2}\frac{d}{d\tau}\|M\|_2^2 \le -\frac{1}{2}\alpha\|M_y\|_2^2 + \delta^2 f^2\left(\|M\|_2 + \frac{1}{2\alpha}\|M\|_2^2\right). \tag{4.10}$$

All M satisfying the boundary conditions (4.5a) also verify a Poincaré inequality

$$b\|M\|_2 \le \|M_y\|_2, \tag{4.11}$$

for some $b > 0$, which together with an application of Young's inequality yields

$$\frac{d}{d\tau}\|M\|_2^2 \le -\left(b^2\alpha - \delta^2 f^2\left(1+\frac{1}{\alpha}\right)\right)\|M\|_2^2 + \delta^4 f^4. \tag{4.12}$$

Lemma 4.1 affords the bound $|f(R)| \le f_\infty = \mathcal{O}(\epsilon)$, so that for δ small enough there exist A and $\kappa > 0$ such that

$$\frac{d}{d\tau}\|M\|_2^2 \le -2\kappa\|M\|_2^2 + A\delta^4\epsilon^4. \tag{4.13}$$

We may integrate (4.13) in τ to obtain

$$\|M(\tau)\|_2 \le A(e^{-\kappa\tau} + \delta^2\epsilon^2), \tag{4.14}$$

for some $A > 0$ independent of δ and ϵ.

To strengthen these decay estimates to the H^1 norm, take the y derivative of (4.4a), multiply by M_y, integrate over $(0,1)$, and integrate by parts to obtain the equality

$$\frac{1}{2}\frac{d}{d\tau}\|M_y\|_2^2 = -\int_0^1 (M+1+\delta f y) M_{yy}^2\, dy + \left(\frac{2}{3}M_y^3 + \delta f M_y^2 + (M+1+\delta f y) M_y M_{yy}\right)\Big|_0^1. \tag{4.15}$$

From Lemma 4.1 we have $C = M + 1 + \delta f y \geq \alpha > 0$, while the boundary condition (4.5a) at $y = 0$ implies $M_\tau(\tau, 0) = 0$ and (4.4a) yields the equality $M_{yy}(\tau, 0) = -(M_y(\tau, 0) + \delta f)^2$. These relations, together with the usual boundary conditions on M, yield the inequality

$$\frac{1}{2}\frac{d}{d\tau}\|M_y\|_2^2 \leq -\alpha\|M_{yy}\|_2^2 + \delta f M_y^2(0) + \frac{1}{3}M_y^3(0) + \delta^2 f^2 M_y(0). \tag{4.16}$$

The L^∞ embedding applied to M_y, the bound $|f| \leq f_\infty = \mathcal{O}(\epsilon)$, and an application of Young's inequality lead to the estimate

$$\frac{1}{2}\frac{d}{d\tau}\|M_y\|_2^2 \leq -\frac{1}{2}\alpha\|M_{yy}\|_2^2 + A\left(\|M_y\|_2^6 + \delta^2\epsilon^2\|M_y\|_2^2 + (\delta^4\epsilon^4\|M_y\|_2)^{2/3}\right). \tag{4.17}$$

We employ Young's inequality on the last term on the right-hand side of (4.17) followed by a Poincaré inequality $\|M_{yy}\|_2 \geq b\|M_y\|_2$, valid for M satisfying the boundary conditions (4.5a), to arrive at the inequality

$$\frac{1}{2}\frac{d}{d\tau}\|M_y\|_2^2 \leq -\left(\frac{1}{4}\alpha b^2 - A\delta^2\epsilon^2\right)\|M_y\|_2^2 + A\left(\|M_y\|_2^6 + \delta^4\epsilon^4\right), \tag{4.18}$$

If δ is small enough, then there exists $\kappa > 0$ such that

$$\frac{1}{2}\frac{d}{d\tau}\|M_y\|_2^2 \leq -\kappa\|M_y\|_2^2 + A\left(\|M_y\|_2^6 + \delta^4\epsilon^4\right). \tag{4.19}$$

For $\|M_y(0)\|_2$ small enough, the right-hand side of (4.19) is initially negative and $\eta = \|M_y\|_2^2$ decays exponentially to the small positive root, $\eta_1 = \mathcal{O}(\delta^4\epsilon^4)$, of the equation $-\kappa\eta_1 + A(\eta_1^3 + \delta^4\epsilon^4) = 0$. From this we deduce the existence of $\kappa, A > 0$ such that

$$\|M_y\|_2 \leq A(e^{-\kappa\tau} + \delta^2\epsilon^2) \qquad \text{for all } \tau \geq 0. \tag{4.20}$$

Since $C_y = M_y + \delta f(R)$, $\|M_y\|_2$ may be chosen small enough if $\|C_y\|_2$ is small and δ is small. Thus δ_0 may depend upon η_0, but η_0 may be taken independent of δ_0. The result (4.7) follows from (4.20) and (4.1a). ∎

4.2. Relaxation of the Reactant Mole Fraction. Due to the small coefficient δ multiplying the diffusive term in (3.1b) the solution R may initially suffer boundary layers; but after a fast transient period, R relaxes to a smooth steady state on the slow time scale measured in $T = \delta\tau$. Unlike the total concentration C, the steady states of R are not well described by the boundary terms, given by R_b in (4.2), and so we must also account for the influence of convection. To this end, we introduce

the adiabatic equation given below, a dynamic reduction of (4.4b) which captures its slow relaxation. Consider the solution U to

$$U_T = F(U(T,1))(U_y - r_2) + U_{yy}, \tag{4.21a}$$

$$U_y(0) = \beta U(0), \qquad U_y(1) = -\epsilon U(1), \tag{4.21b}$$

where $F(z) = f(z + R_b(1))$. We will denote $F(U(T,1))$ by $F(U)$. The nonlinear, nonlocal equation (4.21a) is derived by approximating C in (4.1b) with its quasi-steady state value from (4.7), and then replacing N throughout with U. It is appropriate to supplement (4.21) with the initial condition

$$U(T_0, y) = U_0(y) = R(T_0/\delta, y) - R_b(y), \tag{4.22}$$

where $T_0 > 0$ is specified in Section 4.2.3.

We note that the convective term $F(U)(U_y - r_2)$ in (4.21b) appears at higher order in δ in the anode scaling, while in the cathode scaling it appears at leading order in δ. In this sense we say that the anode is *diffusion-dominated*. This is also reflected in the asymptotics of the steady states derived below.

In the remainder of this section we find the steady states of (4.21), examine the convergence to steady state in the slow time T, and finally show that N and U stay close for all $T \geq T_0$.

4.2.1. Steady States of the Adiabatic Equation. The steady state Φ of (4.21) satisfies the equation

$$\Phi_{yy} + F\Phi_y = r_2 F, \tag{4.23a}$$

$$\Phi_y(0) = \beta\Phi(0), \qquad \Phi_y(1) = -\epsilon\Phi(1), \tag{4.23b}$$

where here and below $F = F(\Phi(1))$. With the integrating factor e^{Fy}, one obtains the following expression for Φ which satisfies (4.23a) and the boundary condition (4.23b) at $y = 1$,

$$\Phi = \Phi_1 + F^{-1}\left(r_2(e^{F(1-y)} - (1 + F(1-y)) + \epsilon\Phi_1(e^{F(1-y)} - 1)\right), \tag{4.24}$$

where $\Phi_1 = \Phi(1)$ The boundary condition at $y = 0$ yields a nonlinear equation for Φ_1,

$$\Phi_1 = r_2\frac{(1 - e^F) + \beta(1 + F - e^F)/F}{\beta + \epsilon e^F - \epsilon\beta(1 - e^F)/F}. \tag{4.25}$$

For the cathode scaling, we replace $\beta = \beta_0\epsilon$ and $\gamma = \gamma_0\epsilon$, and employ a regular expansion for $\Phi_1 = \Phi_1^c$,

$$\Phi_1^c = a_1\epsilon + a_2\epsilon^2 + \cdots. \tag{4.26}$$

A straightforward calculation shows that $a_1 = a_2 = 0$ and

$$\Phi_1^c = \frac{\nu\beta_0^2\gamma_0^2}{\gamma_r(1 + \beta_0)^3}\epsilon^3 + \mathcal{O}(\epsilon^4). \tag{4.27}$$

The solution $\Phi = \Phi^c$ given by (4.24) corresponding to the cathode scaling has the expansion $\Phi^c = \Phi_1^c + \mathcal{O}(\epsilon^4)$, with spatially dependent terms appearing at higher order.

In the anode scaling we substitute $\epsilon = \epsilon_0\delta$ and expand $\Phi_1 = \Phi_1^a$ as

$$\Phi_1^a = b_1\delta + b_2\delta^2 + \cdots, \tag{4.28}$$

which yields

$$\Phi_1^a = \frac{\nu\gamma^2\epsilon_0^2(2+\beta)}{2\beta(\gamma_r - \nu\gamma)}\delta^2 + \mathcal{O}(\delta^3). \tag{4.29}$$

The expansion for the corresponding anode solution $\Phi = \Phi^a$ of (4.23) is

$$\Phi^a = \frac{\nu\gamma^2\epsilon_0^2(2+2\beta y - \beta y^2)}{2\beta(\gamma_r - \nu\gamma)}\delta^2 + \mathcal{O}(\delta^3). \tag{4.30}$$

The expansions of the steady state solutions of (4.23) given by (4.26) and (4.29) are the leading order convective contribution to the limiting states of the reactant equation (3.1b).

4.2.2. Relaxation of the Adiabatic Equation. We address the convergence of the solution U of (4.21) to the steady states Φ found in Section 4.2.1 through the quantity $V = U - \Phi$, which satisfies

$$V_T = F(U)V_y + (F(U) - F(\Phi))(\Phi_y - r_2) + V_{yy}, \tag{4.31a}$$

$$V_y(0) = \beta V(0), \qquad V_y(1) = -\epsilon V(1), \tag{4.31b}$$

$$V(T_0, y) = V_0(y) = U_0(y) - \Phi(y). \tag{4.31c}$$

The following proposition shows that V converges exponentially to zero. In particular this shows that the steady states of (4.21) are stable and unique.

PROPOSITION 4.3. *For δ and ϵ small enough, there exists $\kappa > 0$, independent of δ, ϵ, and $\|V_0\|_{H^1}$, such that the solution V of (4.31) satisfies*

$$\|V\|_{H^1} \le e^{-\kappa T}\|V_0\|_{H^1}, \qquad \text{for all } T \ge T_0. \tag{4.32}$$

Proof. We consider only the cathode scaling; the result for the anode scaling follows with only slight modification to the proof.

Multiply (4.31a) by V, integrate over $(0,1)$, and integrate the last term by parts. There results the equality

$$\frac{1}{2}\frac{d}{dT}\|V\|_2^2 = -\|V_y\|_2^2 + (F(U) - F(\Phi))\int_0^1 (\Phi_y - r_2)V\,dy + \left(\frac{1}{2}F(U)V^2 + VV_y\right)\Big|_0^1. \tag{4.33}$$

It is easy to see from (4.21) that the function $U + R_b(y)$ satisfies the same bounds as R in (4.6). The function F is Lipschitz on $[0, \gamma_1]$ with constant $L = \max\left\{|\epsilon\nu|, \frac{|\epsilon\nu|\gamma_r}{\gamma_r - \nu\gamma_1}\right\} = \mathcal{O}(\epsilon)$. From (4.27) and (4.2) we have the estimate $\|\Phi_y - r_2\|_2 \le A\epsilon^2$ for some $A > 0$. These bounds and the boundary conditions (4.31b) applied to (4.33) lead to the inequality

$$\begin{aligned}\frac{1}{2}\frac{d}{dT}\|V\|_2^2 = &- \|V_y\|_2^2 + AL\epsilon^3|V(1)|\cdot\|V\|_2 \\ &+ \frac{1}{2}|F(U)|\cdot(V(1)^2 + V(0)^2) - \left(\epsilon V^2(1) + \beta V^2(0)\right).\end{aligned} \tag{4.34}$$

Any function V satisfying the boundary conditions (4.31b) obeys the Poincaré inequality $\|V_y\|_2 \geq b\|V\|_2$ for some $b > 0$ if $\epsilon > -\beta/(1+\beta)$, which clearly holds since ϵ and β are both positive. For the boundary terms in (4.34) we use the L^∞ embedding $\|V\|_\infty \leq \sqrt{2}\,\|V_y\|_2^{1/2}\|V\|_2^{1/2} \leq \sqrt{2/b}\,\|V_y\|_2$ and the bound $|F(U)| = \mathcal{O}(\epsilon)$, to obtain an inequality of the form

$$\frac{1}{2}\frac{d}{dT}\|V\|_2^2 \leq -(1 - A\epsilon)\cdot\|V_y\|_2^2. \tag{4.35}$$

For ϵ small enough the Poincaré inequality applied to (4.35) implies the exponential decay of $\|V\|_2$.

To obtain bounds on $\|V_y\|_2$, we simplify the boundary conditions by introducing the linear function $\rho(y) = \beta - y(\epsilon+\beta)$ and the quantity $W = V_y - \rho V$, which satisfies Dirichlet boundary conditions at $y = 0$ and 1. The evolution of W is governed by the equation

$$W_T = F(U)\,(W_y + \rho_y V) + (F(U) - F(\Phi))\cdot(\Phi_{yy} - \rho(\Phi_y - r_2)) + W_{yy} + 2\rho_y V_y. \tag{4.36}$$

From the bound $\|V_y\|_2 \leq \|W\|_2 + \|\rho\|_\infty\cdot\|V\|_2$, we see that the exponential decay of $\|W\|_2$ and $\|V\|_2$ are sufficient to imply the exponential decay of $\|V\|_{H^1}$.

Multiply (4.36) by W, integrate over $(0,1)$, and integrate by parts. From the Dirichlet boundary conditions on W, we derive the inequality

$$\begin{aligned}\frac{1}{2}\frac{d}{dT}\|W\|_2^2 \leq &-\|W_y\|_2^2 + (\epsilon+\beta)\,|F(U)|\cdot\|V\|_2\|W\|_2 \\ &+ |F(U) - F(\Phi)|\cdot\|\Phi_{yy} - \rho(\Phi_y - r_2)\|_2\|W\|_2 + 2|\rho_y|\cdot\|W\|_2\|V\|_2.\end{aligned} \tag{4.37}$$

From (4.27) and (4.2) we obtain the bound $\|\Phi_{yy} - \rho(\Phi_y - r_2)\|_2 \leq A\epsilon^2$ for some $A > 0$. The estimate on the Lipschitz constant for F and the L^∞ embedding yield the following string of inequalities

$$|F(U) - F(\Phi)| \leq L|V(1)| \leq A\epsilon(\|W\|_2^{1/2} + \|V\|_2^{1/2})\cdot\|V\|_2, \tag{4.38}$$

for some $A > 0$. With these bounds, the Poincaré inequality on W, and Young's inequality all applied to (4.37), we obtain an estimate of the form

$$\frac{1}{2}\frac{d}{dT}\|W\|_2^2 \leq -\frac{1}{2}\|W_y\|_2^2 + A\|V\|_2^2, \tag{4.39}$$

for some $A > 0$. The usual Poincaré inequality applied to $\|W_y\|_2$, and the exponential decay of $\|V\|_2$ yield the exponential decay of $\|W\|_2$, and the result (4.32) follows. □

4.2.3. Proximity to the Adiabatic Solution. The solutions C and R of equations (3.1) can be well-approximated by the adiabatic forms defined below in terms of the solution $U(\tau, y) = U(T/\delta, y)$ of (4.21)

$$C^{\mathrm{adb}}(U) = 1 + \delta F(U)\,y, \tag{4.40a}$$

$$R^{\mathrm{adb}}(U) = R_b(y) + U(\tau, y). \tag{4.40b}$$

The initial data (4.22) for U is taken at time $\tau_0 = T_0/\delta$, where τ_0 is large enough that $e^{-\kappa\tau_0} = \mathcal{O}(\delta^2\epsilon^2)$. We may now state and prove our main analytical result.

THEOREM 4.4. *Under the assumptions of Lemma 4.1 and Proposition 4.2, in particular δ and ϵ small enough, the solutions C and R given by (4.1) through (4.4) are approximated by the adiabatic forms (4.40) in the sense that*

$$\|C - C^{\mathrm{adb}}(U)\|_{H^1} \leq A(e^{-k\tau} + \delta^2\epsilon^2), \qquad \text{for all } \tau \geq 0, \tag{4.41a}$$

$$\|R - R^{\mathrm{adb}}(U)\|_{H^1} \leq A\delta\epsilon, \qquad \text{for all } \tau \geq \tau_0, \tag{4.41b}$$

for some $A, \kappa > 0$.

Proof. We consider only the cathode scaling; the arguments for the anode scaling require only minor modifications. Since $R = R_b + N$ where N satisfies (4.1b), we prove (4.41b) by bounding the quantity $E = N - U$, whose evolution is governed by the equation

$$E_\tau = (C + \delta \ln C)_y E_y + [(C + \delta \ln C)_y - \delta F(U)] \cdot (U_y - r_2) + \delta E_{yy}. \tag{4.42}$$

Moreover, E satisfies the same homogeneous boundary conditions as N in (4.5b), and has zero initial data at $\tau = \tau_0$. In light of Proposition 4.2 we have the estimate

$$\|C - (1 + \delta F(U)y)\|_{H^1} \leq A\left(e^{-\kappa\tau} + \delta^2\epsilon^2 + \delta|F(U) - F(N)|\right). \tag{4.43a}$$

The function F is Lipschitz on the range of U and N with Lipschitz constant $L = \mathcal{O}(\epsilon)$. This implies

$$|F(U) - F(N)| \leq A\epsilon\|E\|_\infty, \tag{4.44}$$

and so we find

$$\|C - (1 + \delta F(U)y)\|_{H^1} \leq A\left(\delta^2\epsilon^2 + \delta\epsilon\|E\|_\infty\right), \qquad \text{for all } \tau \geq \tau_0. \tag{4.45}$$

To obtain bounds on $\|E\|_2$ we multiply (4.42) by E, integrate over $(0,1)$, and integrate the last term by parts, from which follows the equality

$$\frac{1}{2}\frac{d}{d\tau}\|E\|_2^2 = \int_0^1 \Big((C + \delta \ln C)_y E_y E + [(C + \delta \ln C)_y - \delta F(U)] \cdot (U_y - r_2)E - \delta E_y^2\Big)\, dy - (\epsilon + \beta)E^2\big|_0^1. \tag{4.46}$$

From Proposition 4.2 we have the bound

$$\|(C + \delta \ln C)_y\|_2 \leq A\delta|f(R)| \leq A\delta\epsilon, \qquad \text{for all } \tau \geq \tau_0. \tag{4.47}$$

In particular $\|\delta(\ln C)_y\|_2 = \delta\|C_y/C\|_2 \leq A\delta^2\epsilon$. This inequality together with (4.45) yields

$$\begin{aligned}\|(C + \delta \ln C)_y - \delta F(U)\|_2 &\leq \|C_y - \delta F(U)\|_2 + \delta\|C_y/C\|_2, \\ &\leq A\delta\epsilon(\delta + \|E\|_\infty).\end{aligned} \tag{4.48}$$

We drop the negative boundary terms in (4.46) and employ the estimates (4.47), (4.48), and Hölder's inequality to find

$$\frac{1}{2}\frac{d}{d\tau}\|E\|_2^2 \leq -\delta\|E_y\|_2^2 + A\delta\epsilon\Big(\|E_y\|_2\|E\|_\infty + (\delta + \|E\|_\infty) \cdot (\|U_y\|_2 + r_2) \cdot \|E\|_\infty\Big). \tag{4.49}$$

Rescale time to $T = \delta\tau$, use the L^∞ embedding and Poincaré inequality on E, and Young's inequality on terms linear in E to obtain an estimate of the form

$$\frac{d}{dT}\|E\|_2^2 \leq -\left(\frac{1}{2} - A\epsilon(\|U_y\|_2^2 + 1)\right)\|E_y\|_2^2 + A\delta^2\epsilon^2(\|U_y\|_2^2 + 1), \tag{4.50}$$

for some $A > 0$. Proposition 4.3 implies that $\|U_y\|_2$ is uniformly bounded, independent of δ for $T \geq T_0$. For ϵ small enough it follows from Poincaré's inequality that the solution E of (4.42), with zero initial data at $T = T_0$ satisfies

$$\|E\|_2 \leq A\delta\epsilon \qquad \text{for all } T \geq T_0. \tag{4.51}$$

To extend these results to the H^1 norm, we introduce the quantity $\widetilde{W} = E_y - \rho E$ which satisfies Dirichlet boundary conditions at $y = 0$ and $y = 1$. Since $\widetilde{W}_\tau = E_{\tau y} - \rho E_\tau$, we may combine (4.42) with its y derivative to obtain the following evolution equation for $\widetilde{W}$,

$$\begin{aligned}\widetilde{W}_\tau =&(C + \delta\ln C)_{yy}E_y + (C + \delta\ln C)_y(\widetilde{W}_y + \rho_y E) + ((C + \delta\ln C)_y - \delta F(U))_y\,(U_y - r_2)\\ &+ ((C + \delta\ln C)_y - \delta F(U))\cdot(U_{yy} - \rho U_y + \rho r_2) + \delta\widetilde{W}_{yy} + 2\delta\rho_y E_y.\end{aligned} \tag{4.52}$$

Multiply (4.52) by W, integrate over $(0,1)$, and integrate by parts on the first, third, fifth, and sixth terms on the right-hand side, to obtain the equality

$$\begin{aligned}\frac{1}{2}\frac{d}{d\tau}\|\widetilde{W}\|_2^2 =& \int_0^1 \Big\{(C + \delta\ln C)_y(\widetilde{W}\widetilde{W}_y + \rho_y E\widetilde{W} - (E_y\widetilde{W})_y)\\ &- ((C + \delta\ln C)_y - \delta F(U))\cdot\Big((U_y - r_2)\cdot(\rho\widetilde{W} + \widetilde{W}_y)\Big)\Big\}\,dy\\ &- \delta\|\widetilde{W}_y\|_2^2 - 2\delta\rho_y\int_0^1 E\widetilde{W}_y dy.\end{aligned} \tag{4.53}$$

The integrand of the first integral on the right-hand side of (4.53) is comprised of two terms. The first factor of the first term is estimated by (4.47), while the second factor is dominated by the term $(E_y\widetilde{W})_y$. We estimate

$$\|(E_y\widetilde{W})_y\|_2 \leq \|E_{yy}\|_2\|\widetilde{W}\|_\infty + \|E_y\|_\infty\|\widetilde{W}\|_2, \tag{4.54}$$

and from the triangle inequality, the L^∞ embedding applied to, E, and Poincaré applied to W it follows that

$$\|E_{yy}\|_2 + \|E_y\|_\infty \leq A(\|\widetilde{W}_y\|_2 + \|E\|_2), \tag{4.55a}$$

$$\|E_y\|_2 + \|E\|_\infty \leq A(\|\widetilde{W}\|_2 + \|E\|_2). \tag{4.55b}$$

The inequalities (4.54) and (4.55), together with an application of Young's inequality, lead to the estimate

$$\|(E_y\widetilde{W})_y\|_2 \leq A(\|\widetilde{W}_y\|_2^2 + \|E\|_2^2). \tag{4.56}$$

The first factor of the second term of the integrand of (4.52) is bounded by the estimate (4.48). From arguments similar to those used to derive (4.56), we find an estimate on the second factor of the second term of the form

$$\|(U_y - r_2)\cdot(\rho\widetilde{W} + \widetilde{W}_y)\|_2 \leq A\,(\|U_y\|_2 + 1)\cdot\|\widetilde{W}_y\|_2. \tag{4.57}$$

Then, rescaling time by $T = \delta\tau$, and applying Hölder's inequality and the estimates gathered above, we obtain an inequality of the form

$$\frac{1}{2}\frac{d}{dT}\|\widetilde{W}\|_2^2 \leq -\|\widetilde{W}_y\|_2^2 + A\epsilon\Big(\|\widetilde{W}_y\|_2^2 + \|E\|_2^2 + (\delta + \|\widetilde{W}\|_2 + \|E\|_2)\cdot(\|U_y\|_2 + 1)\cdot\|\widetilde{W}_y\|_2\Big). \tag{4.58}$$

We employ the bound $\|E\|_2 \leq A\delta\epsilon$ from (4.51) and use Poincaré on $\widetilde{W}$ and Young's inequality on all terms linear in $\|\widetilde{W}\|_2$ to combine the $\widetilde{W}_y$ dependent terms on the right-hand side of (4.58) into one term quadratic in $\|\widetilde{W}_y\|_2$. For ϵ small enough, the sign of this later term is negative, and applying Poincaré to $\widetilde{W}$ we obtain an inequality of the form

$$\frac{d}{dT}\|\widetilde{W}\|_2^2 \leq -2\kappa\|\widetilde{W}\|_2^2 + A\delta^2\epsilon^2(\|U_y\|_2^2 + 1), \tag{4.59}$$

for some κ and A positive and independent of δ and ϵ small enough. Since $\|U_y\|_2$ is uniformly bounded for $T \geq T_0$ and $\widetilde{W}$ has zero initial data at $T = T_0$, integration of (4.59) over the time interval (T_0, T) yields the bound

$$\|\widetilde{W}(T)\|_2 \leq A\delta\epsilon, \qquad \text{for all } T \geq T_0, \tag{4.60}$$

and for some $A > 0$ independent of ϵ and δ. The result (4.41b) follows immediately from (4.51), (4.60), and the inequality (4.55b), while (4.41a) follows from (4.41b), (4.45), and Proposition 4.2. ∎

4.3. Limiting states of the Anode and Cathode Scalings. Theorem 4.4 indicates that the steady state solutions of the adiabatic equations (4.21), given for the anode and cathode scalings in Section 4.2.1, describe the limiting behavior of the full system as $\tau \to \infty$. Indeed from Theorem 4.4 and Proposition 4.3 we have immediately

COROLLARY 4.5. *Under the assumptions of Theorem 4.4, for the steady state solution Φ of (4.23)*

$$\limsup_{\tau\to\infty} \|C - C^{\mathrm{adb}}(\Phi)\|_{H^1} \leq A\delta^2\epsilon^2, \tag{4.61a}$$

$$\limsup_{\tau\to\infty} \|R - R^{\mathrm{adb}}(\Phi)\|_{H^1} \leq A\delta\epsilon. \tag{4.61b}$$

For the anode scaling, using $\Phi = \Phi^a$ from (4.30) and the definition of C^{adb} and R^{adb} from (4.40), it is straightforward to obtain an expansion for the limiting states of total concentration and reactant

$$C^{\mathrm{adb}}(\Phi) = 1 - \left(\epsilon_0\frac{\nu\gamma y}{\gamma_r - \nu\gamma}\right)\delta^2 + \mathcal{O}(\delta^3), \tag{4.62a}$$

$$R^{\mathrm{adb}}(\Phi) = \gamma - \epsilon_0\gamma(y + 1/\beta)\delta + \mathcal{O}(\delta^2), \tag{4.62b}$$

valid to within the error of Corollary 4.5. More importantly, from (3.3) we can approximate asymptotically the net flux N_1 of reactant into the catalyst layer at $y = 1$ as

$$N_1 = \frac{\epsilon_0\gamma\gamma_r}{\gamma_r - \nu\gamma}\,\delta^2 + \mathcal{O}(\delta^3). \tag{4.63}$$

In dimensional variables this expression takes the form

$$N_1^d = \overline{C}_1 r_{_H} \left(\frac{\overline{C}_1 + \overline{C}_2}{(1-\nu)\overline{C}_1 + \overline{C}_2} \right) + \frac{\Gamma \overline{C}^2}{H} \mathcal{O}(\delta^3), \tag{4.64}$$

where we observe from Table 3.1 that $\Gamma\overline{C}^2/H \sim \mathcal{O}(1.0\ mol/cm^2 \cdot s)$. In the anode scaling, the transfer coefficient $r_{_H}$ is the limiting element (*i.e.*, $r_{_H} \ll r_{_0}$), and we find that the flux depends only upon $r_{_H}$, the return coefficient ν, and the channel reactant concentration $\overline{C}_1$.

For the cathode scaling, using the expression $\Phi = \Phi^c = \Phi_1^c + \mathcal{O}(\epsilon^4)$ from (4.27) we expand the limiting states in ϵ to find

$$C^{\mathrm{adb}}(\Phi) = 1 - \frac{\nu\beta_0\gamma_0}{(1+\beta_0)\gamma_r} \left(\epsilon^2 - \frac{\beta_0(\gamma_r - \gamma_0\nu)}{(1+\beta_0)\gamma_r} \epsilon^3 \right) y\delta + \mathcal{O}(\epsilon^4\delta, \delta^2), \tag{4.65a}$$

$$R^{\mathrm{adb}}(\Phi) = \frac{\beta_0\gamma_0}{1+\beta_0} \left[\epsilon - \left(y - \frac{1}{1+\beta_0} \right) \epsilon^2 + \frac{\beta_0}{(1+\beta_0)\gamma_r} \left(\gamma_r y - \frac{\gamma_r - \gamma_0\nu}{1+\beta_0} \right) \epsilon^3 \right] + \mathcal{O}(\epsilon^4). \tag{4.65b}$$

The net flux for the cathode takes the dimensionless form

$$N_1 = \frac{\beta_0\gamma_0}{1+\beta_0} \left(\epsilon^2 - \frac{\beta_0(\gamma_r - \gamma_0\nu)}{(1+\beta_0)\gamma_r} \epsilon^3 \right) \delta + \mathcal{O}(\epsilon^4\delta, \delta^2). \tag{4.66}$$

In dimensional variables, we may express the flux in the appealing form

$$N_1^d = \overline{C}_1 r_e \left(1 + \frac{\overline{C}_1 \nu r_{_0}}{(\overline{C}_1 + \overline{C}_2)(r_{_0} + r_{_H})} - \frac{H}{D} r_e \right) + \frac{\Gamma \overline{C}^2}{H} \mathcal{O}(\epsilon^4\delta, \delta^2), \tag{4.67}$$

where the effective transfer coefficient, $r_e \equiv (1/r_{_0} + 1/r_{_H})^{-1}$, is the reciprocal sum of the individual transfer coefficients $r_{_0}$ and $r_{_H}$.

The net flux of reactant depends only upon the transfer rates at top and bottom, concentrations in the channel, return coefficient ν, diffusivity, and GDL thickness. The permeability is not evident here, occurring at higher order in the expansion of N_1^d. Moreover, the diffusivity and GDL thickness occur only through the dimensionless combination $\frac{H}{D} r_e = \mathcal{O}(\epsilon)$, which is a small correction to the leading order term. We expect the diffusivity to appear at first order in a two-dimensional problem with flow channels if the channel aspect ratio L_c/L is not small.

Remarks: (1) We can recover the anode result to leading order by taking $r_{_H} \ll r_{_0}$ and expanding $(1-\nu\gamma)^{-1} \sim 1 + \nu\gamma + \ldots$. (2) For the cathode $\nu < 0$ and formula (4.67) demonstrates the sub-linear response of flux (and hence also current density) to increasing O_2 channel concentration $\overline{C}_1$. This effect is present in our one-dimensional model and is associated with convective terms.

5. Numerical Comparisons. We now give a brief overview of the numerical method we employed for solving the two-dimensional GDL equations. A complete description of the code, including a study of convergence, stability and parameter sensitivities, is provided in [21].

The dimensional system (2.2)–(2.6) is discretized in space using a finite volume approach, which is a natural choice in view of the mass conservation properties of the continuous problem. The rectangular domain is divided into a uniform, $nx \times ny$ mesh with grid spacings $\Delta x^d = L/nx$ and $\Delta y^d = H/ny$ (the superscript "d" denotes

dimensional length measurements to avoid confusion with the nondimensional grid spacing $\Delta y = 1/ny$). The concentrations C and C_1 and pressure P are cell-averaged quantities located at cell centers, while the vector-valued velocities and fluxes are defined as edge averages. Centered differences are used to approximate derivatives so that the resulting discretization is second order accurate in the grid spacing. The boundary conditions are also approximated by centered differences, with "fictitious cells" being used for points lying outside the domain. Solution values at fictitious points are approximated using second-order extrapolation from interior points so that the overall scheme retains second order accuracy up to the boundary.

After spatial discretization, we are left with a large, time-dependent, nonlinear system of ordinary differential equations to solve at each grid point. Furthermore, the system is stiff, as indicated by the presence of two widely disparate time scales in our convergence analysis of Section 4. Consequently, we have chosen to use the stiff differential–algebraic system solver DASSL [15] to integrate the solution in time. DASSL uses a variable-order BDF method with adaptive time-stepping which provides an accurate and efficient computation of the solution, as outlined in the next section.

5.1. Stiffness. The presence of a fast and slow time scale, discussed in the previous analysis, suggests a very stiff problem for which explicit time-stepping methods can be highly inefficient. A small step is required for accurate resolution of initial, rapidly-varying transients, but is unjustified at later times when the transients have died out and the solution relaxes adiabatically to steady state on the slow time scale. We have implemented an explicit, forward Euler version of the code, which for a typical GDL simulation on a 34×24 grid requires over 10^9 time steps to reach steady state (corresponding to a fixed time step of $\Delta t \approx 10^{-9}\ s$) and which was quite computationally intensive. In contrast, the implicit, variable time-stepping method in DASSL provided a dramatic improvement in performance. Clearly, the stiffness in the GDL problem is severe enough that use of an implicit method is required for practicality. This situation can only be further complicated in a larger coupled system for the entire fuel cell.

The severity of the time step restriction is due primarily to the porous medium equation which defines the velocity as a derivative of the concentration, so that the convective terms in Eqs. (2.7) actually appear as diffusive terms. The time step restriction for diffusive problems takes the form $\Delta t \leq (\Delta y^d)^2/(2D)$, while the presence of a convective term usually introduces a CFL-type restriction of the form $\Delta t \leq \Delta y^d/U_{max}$. For our GDL model however, the convective terms appear as second derivatives multiplied by a coefficient $(\Gamma\overline{C})$ or $(\Gamma\overline{C}_1)$. The time step restriction for our problem, written in dimensional variables, has the form

$$\Delta t \leq \frac{(\Delta y^d)^2}{2} \min\left\{\frac{1}{D}, \frac{1}{\Gamma\overline{C}}, \frac{1}{\Gamma\overline{C}_1}\right\}. \tag{5.1}$$

With the anode parameter values from Table 3.1 (and $ny = 24$ so that $\Delta y^d \approx 0.002\ cm$), this time step restriction becomes $\Delta t < 8 \times 10^{-9}$, with a limit of only $\Delta t < 6 \times 10^{-6}$ arising from the diffusion term. Similar values are obtained at the cathode. The stability restrictions arising from this simple linear argument give a very close match to the time steps required for explicit computations of the full fuel cell system. The reduced, adiabatic equation (4.21) on the other hand, has a time step limited by diffusion only, which translates into a thousand-fold speed-up for an explicit method.

We can also rewrite the time step restriction in terms of non-dimensional variables for both the fast and slow time scales $\tau = (\Gamma\overline{C}/H^2)\,t$ and $T = (D/H^2)\,t$:

$$\Delta\tau \leq \frac{(\Delta y)^2}{2}\min\left\{\frac{1}{\delta}, 1, \frac{1}{\gamma}\right\} \quad \textit{(fast)} \qquad \text{and} \qquad \Delta T \leq \frac{(\Delta y)^2}{2}\min\left\{1, \delta, \frac{\delta}{\gamma}\right\} \quad \textit{(slow)}.$$

Realizing that $\delta \ll 1$ and $\gamma \lesssim 1$, it is clear that these conditions reduce to $\Delta\tau \leq (\Delta y)^2/2$ and $\Delta T \leq \delta(\Delta y)^2/2$, clearly indicating that diffusive effects only limit the slow time scale T.

5.2. Validation of 1D Steady State Results. In this section, we present numerical results that validate the analytical formulae for the steady state solutions, and the adiabatic portion of the convergence. The computations are performed on a "quasi-1D" problem with the channel and solid wall at the lower boundary replaced by a uniformly porous surface, which corresponds to taking $L_c = L$ in the notation introduced in Fig. 2.2. Because of the resulting symmetry in the domain and boundary conditions, the solution is independent of x and so that a vertical, mid-channel cross-section of the computed results can be readily compared to the analytical solution. All results that follow are reported in non-dimensional variables, except where otherwise noted.

We begin by comparing the computed mixture concentration and reactant mole fraction with the "exact" steady state obtained numerically from the 1D steady state version of (3.1), and also with the asymptotic solution from either of Eqs. (4.62) or (4.65). The parameters used for both electrodes are listed in Table 3.1. The results for the anode and cathode are presented separately in Figs. 5.1 and 5.2 respectively, from which it is clear that both analytical results match extremely well with the computations. Furthermore, all curves exhibit the expected linear (or near-linear) dependence on y that is observed in computations in higher dimensions.

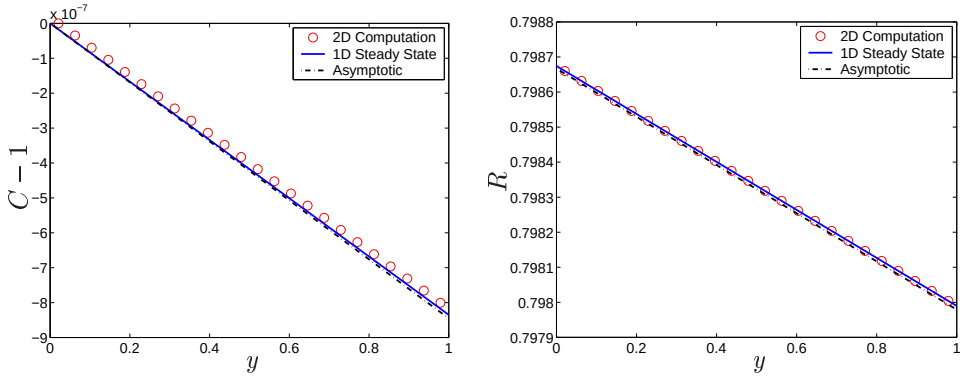

(a) Anode mixture concentration. *(b) Anode reactant mole fraction.*

FIG. 5.1. *Comparison of the computed concentration* $(C-1)$ *and mole fraction* $R = C_1/C$ *with theoretical predictions for the anode* (H_2 *side). The parameters are taken from Table 3.1, and the computations performed on a* 32×48 *grid.*

We next investigate numerically the nature of convergence to steady state and draw comparisons with the analytical results derived in Section 4. Fig. 5.3(a) shows

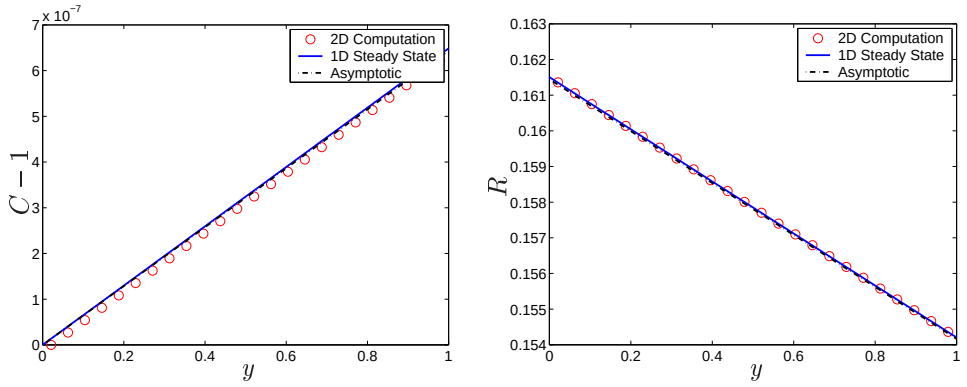

(a) Cathode mixture concentration. *(b) Cathode reactant mole fraction.*

FIG. 5.2. *Comparison of the computed concentration C and mole fraction $R = C_1/C$ with theoretical predictions for the cathode (O_2 side). The parameters are taken from Table 3.1, and the computations performed on a 32×48 grid.*

the variation of concentration profiles with time, starting from the initial profiles $C \equiv 1$ and $R \equiv \gamma$. The initially horizontal concentration curve relaxes over a short time interval (of approximately 10^{-5} s) to a linear profile, which is very close to the final steady state. The solution then enters the adiabatic regime, in which the curve remains linear and relaxes to the steady state on the slow time scale. The concentration actually overshoots the steady state solution, with the slope reaching a maximum shortly after $t = 10^{-5}$ s (*i.e.*, $\tau \approx 3.0$ and $T \approx 0.0005$), following which the steady state is approached from below. This adiabatic behavior is best conveyed by Fig. 5.4(a) which plots the slope of the solution profile versus time for the anode and cathode concentrations. In this figure, we present numerical solutions of both the original system (3.1)–(3.2) and the adiabatic equation (4.21) derived from (4.3). The "slope," computed using the divided difference $(C(1) - C(0))/(1 - 0)$, is an accurate representation of the curves during the adiabatic phase, but only yields an approximation during the initial transient regime when the profiles are nonlinear. Notice that the concentration slope at the cathode is positive, due to the inflow of water vapor at the upper boundary with a positive return coefficient $\nu = 0.99$.

In Fig. 5.3(b), we show profiles of the anode mole fraction, which lacks a rapid convective transient, and consequently the adiabatic variation is much more pronounced. In contrast with the concentration curves, the relaxation of R to its steady state is monotonic, as is easily seen in the plots of slope versus time in Fig. 5.4(b).

5.3. Two-Dimensional Computations. The one-dimensional results of the previous section are strong evidence to support our asymptotic approximations to the GDL model. In most fuel cell applications, geometric constraints render the flow fundamentally two-dimensional. In this section, we present simulations of flow through more realistic two-dimensional geometry as depicted in Fig. 2.2, and demonstrate how the one-dimensional asymptotic results are useful in predicting certain flow quantities.

Fig. 5.5 shows a representative computation, with plots of mole fraction and total hydrogen flux for the case $L_c/L = 0.5$. While the variation in R is nearly linear along

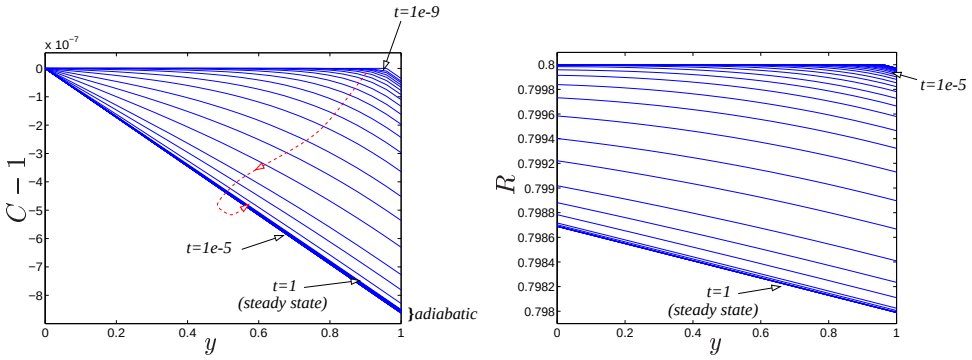

(a) Anode mixture concentration. *(b) Anode mole fraction.*

FIG. 5.3. *Convergence to steady state of the anode mixture concentration and mole fraction. The curves are displayed at 50 time steps between 10^{-9} and 5.0, equally-spaced on a log scale. In the transient, convective regime the mixture concentration moves very rapidly to a linear profile that overshoots the steady state. There follows an adiabatic relaxation on the slow time scale to the steady state. The mole fraction on the other hand has no fast transient and relaxes entirely on the slow time scale.*

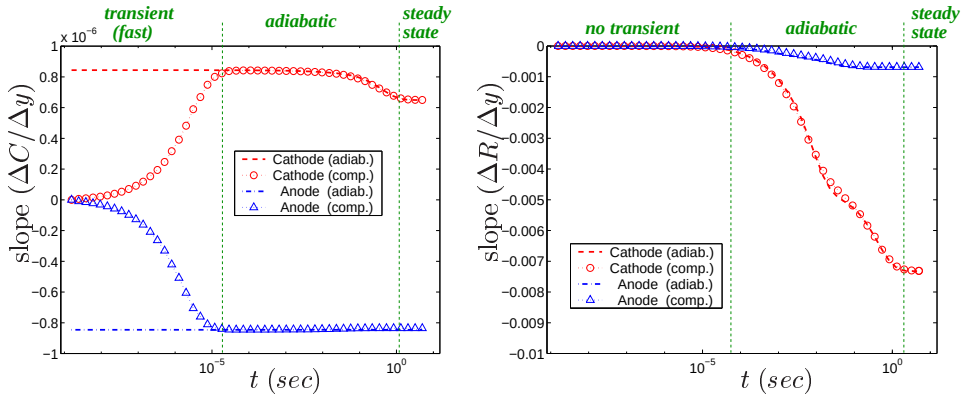

(a) Slope of concentration curves exhibits a fast initial transient, followed by a slow adiabatic relaxation to the steady state.

(b) Slope of mole fraction curves exhibits a similar adiabatic relaxation to the steady state, but no fast transient.

FIG. 5.4. *Comparison of the computed and adiabatic solutions, in terms of the slope of the C and R curves versus dimensional time. The asymptotic, adiabatic equations capture the steady state and the slow relaxation.*

vertical cross-sections ($x = constant$), there is a significant two-dimensional effect due to variation along the x–direction, which is also evident in the flux vector plot in Fig. 5.5(b).

To measure the departure of the two-dimensional solution from one-dimensionality we vary the channel aspect ratio L_c/L, with L fixed, focusing our attention on the flux of reactant along the top wall, $N_1|_{y=H}$. This quantity has very important physical

implications, being related to the reactant consumption rate and thus also to current density, which is a primary measure of fuel cell performance. Fig. 5.6(a) contains plots of the top wall flux as a function of x for aspect ratios between 0.2 and 1.0, with the domain length fixed at $L = 1.0$. The asymptotic flux from (4.64) is plotted as a dashed line for comparison purposes. While there is significant variation in the overall flux, the peak flux at mid-channel remains virtually fixed and the asymptotic approximation to the peak flux is accurate to within an error of 2%, even when the channel aspect ratio is as small as 0.4. It is only when the aspect ratio is reduced below 0.4 that an appreciable drop in maximum flux appears.

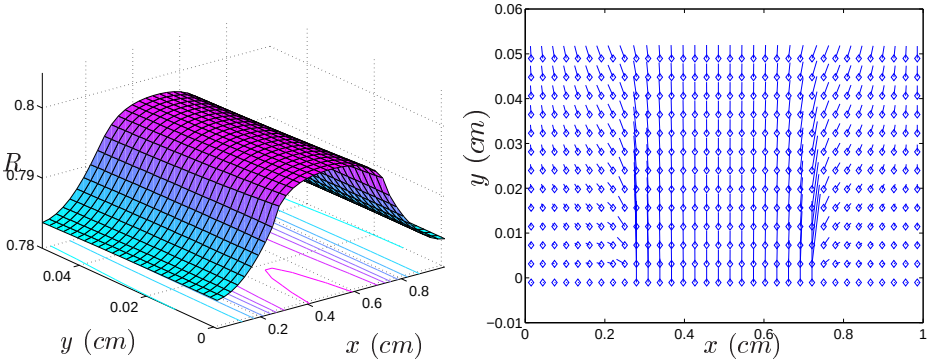

(a) Anode reactant mole fraction. *(b) Anode total reactant flux, N_1^d.*

FIG. 5.5. *Plots of reactant mole fraction and total flux for a two-dimensional anode simulation with $L_c/L = 0.5$ (in dimensional variables).*

Experimental evidence suggests that changing channel geometry influences fuel cell performance by affecting electrical contacts and water flooding [14]. We have thus demonstrated a third factor that influences performance – namely mass transport limitations.

A central result of our one-dimensional asymptotic analysis is that the top wall flux (4.64) at the anode does not depend on parameters such as the diffusivity or permeability, to lowest order in δ. This has implications in terms of the design of new GDL materials. While the diffusivity is an intrinsic property of the gas that does not vary, it is technically not the diffusivity D that appears in (2.7b) but rather an *effective diffusivity* D^{eff}, which is often related to D in the porous media literature via the semi-empirical formula $D^{eff} = \varepsilon_p^{1.5} D$, known as the *Bruggeman correction*. We are therefore justified in considering the effect of variation in D on the reactant flux. The results are displayed in Fig. 5.6(b), from which it is clear that the maximum flux has little sensitivity to the diffusivity, even in a two-dimensional calculation.

6. Conclusions. By considering each electrode of the fuel cell in isolation, and replacing the coupling to the rest of the fuel cell system with appropriate boundary conditions, we develop a model for multicomponent gas transport within an electrode which is amenable to analysis. The system of convection–diffusion equations we present captures qualitatively the fundamental physical phenomena appearing in more complicated models of the entire fuel cell. Moreover, we identify distinct scal-

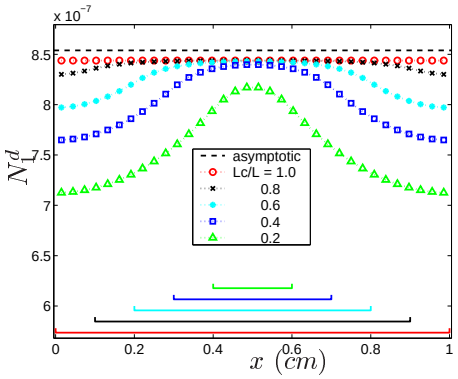

(a) Flux profiles for various channel aspect ratios. The size and location of the channels for each value of L_c/L are indicated with solid lines at the bottom.

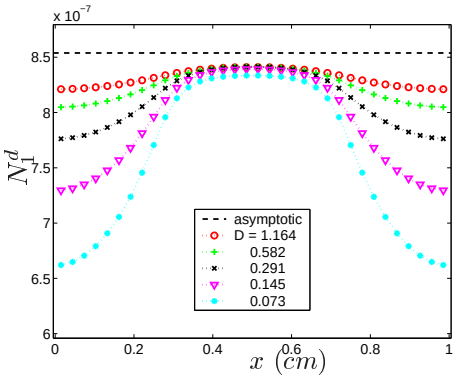

(b) Flux profiles for various diffusivity values. The channel aspect ratio is held constant at 0.5.

FIG. 5.6. *Plots of the dimensional top wall reactant flux N_1^d at the anode as the channel aspect ratio, L_c/L, or the diffusivity, D, are varied.*

ings of the problem variables which describe the different operating conditions at the anode and cathode.

For a one-dimensional problem we present asymptotic expansions of the steady state solutions which demonstrate the functional dependence upon material parameters. We also derive a reduced system that describes the adiabatic portion of the two-scale relaxation onto the steady state. This reduced system eliminates the numerical stiffness associated with the fast time scale, while qualitatively reproducing the diffusive transients which have application to dynamic fuel cell performance. Significant computational benefit should be achievable by incorporating some form of this reduced system into full fuel cell simulations.

The extension of our analysis to two space dimensions is possible. Indeed, we show that the one-dimensional model retains its predictive power in a two-dimensional geometry, accurately describing the peak reactant flux and demonstrating its lack of dependence upon parameters such as the diffusivity. Our preliminary numerical simulations which include the Maxwell–Stefan equations [12] for the diffusive fluxes show only a very small quantitative difference from those presented here.

Future work includes modeling temperature variations within the GDL and the multiphase flow resulting from liquid water condensation, relating to issues of water management. A coupled anode–cathode model that incorporates elements from the PEM and the catalytic reaction rates would be of great value to the fuel cell industry.

Acknowledgments. We would like to thank John Kenna and Greg James of Ballard Power Systems in Burnaby, BC for many helpful discussions and their willingness to provide experimental data. We are also indebted to Huaxiong Huang, Brian Wetton, and the other members of the Mathematical Modeling and Scientific Computation Group of MITACS for their help in the early development of the electrode model. We are particularly thankful to the referees for their suggestions which led to substantial improvements in the presentation of results.

REFERENCES

[1] L. M. Abriola and G. F. Pinder. A multiphase approach to the modeling of porous media contamination by organic compounds. 1. Equation development. *Water Resour. Res.*, 21(1):11–18, 1985.

[2] S. Ahn and B. J. Tatarchuk. Fibrous metal-carbon composite structures as gas diffusion electrodes for use in alkaline electrolyte. *J. Appl. Electrochem.*, 27:9–17, 1997.

[3] H. D. Baehr and K. Stephan. *Heat and Mass Transfer*. Springer-Verlag, Berlin, 1998.

[4] D. M. Bernardi and M. W. Verbrugge. A mathematical model of the solid-polymer-electrolyte fuel cell. *J. Electrochem. Soc.*, 139(9):2477–2491, 1992.

[5] R. B. Bird, W. E. Stewart, and E. N. Lightfoot. *Transport Phenomena*. John Wiley & Sons, New York, 1960.

[6] Y. G. Chirkov, V. I. Rostokin, and A. G. Pshenichnikov. The influence of the porous electrode structure on the gas generation modes. *Russ. J. Electrochem.*, 32(9):1009–1016, 1996.

[7] R. E. Cunningham and R. J. J. Williams. *Diffusion in Gases and Porous Media*. Plenum Press, New York, 1980.

[8] A. Friedman and S. Kamin. The asymptotic behavior of gas in an n-dimensional porous medium. *Trans. Amer. Math. Soc.*, 262(2):551–563, 1980.

[9] V. Gurau, H. Liu, and S. Kakaç. Two-dimensional model for proton exchange membrane fuel cells. *AIChE J.*, 44(11):2410–2422, 1998.

[10] A. S. Kalashnikov. Some problems of the qualitative theory of non-linear degenerate second-order parabolic equations. *Russ. Math. Surveys*, 42(2):169–222, 1987.

[11] D. L. Koch, R. G. Cox, H. Brenner, and J. F. Brady. The effect of order on dispersion in porous media. *J. Fluid Mech.*, 200:173–188, 1989.

[12] R. Krishna. Problems and pitfalls in the use of the Fick formulation for intraparticle diffusion. *Chem. Eng. Sci.*, 48(5):845–861, 1993.

[13] F. J. Mancebo and J. M. Vega. Weakly nonuniform thermal effects in a porous catalyst: Asymptotic models and local nonlinear stability of the steady states. *SIAM J. Appl. Math.*, 52(5):1238–1259, 1992.

[14] V. A. Paganin, E. A. Ticianelli, and E. R. Gonzalez. Development and electrochemical studies of gas diffusion electrodes for polymer electrolyte fuel cells. *J. Appl. Electrochem.*, 26:297–304, 1996.

[15] L. R. Petzold. A description of DASSL: A differential/algebraic system solver. Technical Report SAND82–8637, Sandia National Laboratories, Sept. 1982.

[16] M. H. Protter and H. F. Weinberger. *Maximum Principles in Differential Equations*. Springer-Verlag, 1984.

[17] K. R. Rajagopal. An introduction to mixture theory. In G. P. Galdi, J. Málek, and J. Nečas, editors, *Mathematical Theory in Fluid Mechanics*, pages 86–113. Longman, 1996.

[18] J. Salles, J.-F. Thovert, R. Delannay, L. Prevors, J.-L. Auriault, and P. M. Adler. Taylor dispersion in porous media. Determination of the dispersion tensor. *Phys. Fluids A*, 5(10):2348–2376, 1993.

[19] D. Singh, D. M. Lu, and N. Djilali. A two-dimensional analysis of mass transport in proton exchange membrane fuel cells. *Int. J. Engrg. Sci.*, 37:431–452, 1999.

[20] B. E. Sleep and J. F. Sykes. Compositional simulation of groundwater contamination by organic compounds. 1. Model development and verification. *Water Resour. Res.*, 29(6):1697–1708, 1993.

[21] J. M. Stockie. Numerical simulation of multicomponent gas transport in anisotropic porous electrodes. In preparation, 1999.

[22] R. Taylor and R. Krishna. *Multicomponent Mass Transfer*. Wiley Series in Chemical Engineering. John Wiley & Sons, 1993.

[23] J. A. Trangenstein and J. B. Bell. Mathematical structure of the black-oil model for petroleum reservoir simulation. *SIAM J. Appl. Math.*, 49(3):749–783, 1989.

[24] J. L. Vazquez. An introduction to the mathematical theory of the porous medium equation. In M. C. Defour, editor, *Shape Optimization and Free Boundaries*, volume 380 of *NATO ASI Series C: Mathematical and Physical Sciences*, pages 347–389. Kluwer, Dordrecht, 1992.

[25] N. E. Wijeysundera, B. F. Zheng, M. Iqbal, and E. G. Hauptmann. Numerical simulation of the transient moisture transfer through porous insulation. *Int. J. Heat Mass Transfer*, 39(5):995–1004, 1996.

[26] J. S. Yi and T. V. Nguyen. Multicomponent transport in porous electrodes of proton exchange membrane fuel cells using the interdigitated gas distributors. *J. Electrochem. Soc.*, 146(1):38–45, 1999.